J. Fluid Mech. (2022), *vol*. 940, A18, doi:10.1017/jfm.2022.250

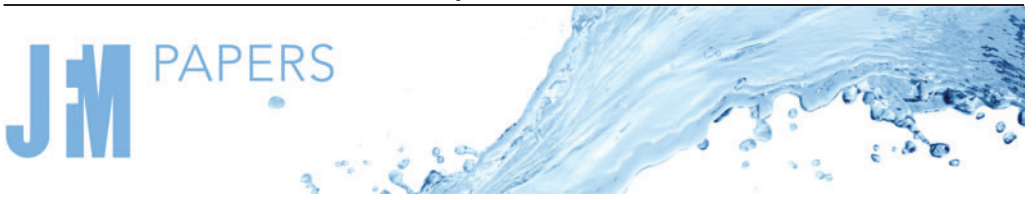

Helicity distributions and transfer in turbulent channel flows with streamwise rotation

Changping Yu[1], **Running Hu**[1,2], **Zheng Yan**[3,†] **and Xinliang Li**[1,2,†]

[1]LHD, Institute of Mechanics, Chinese Academy of Sciences, Beijing 100190, PR China

[2]School of Engineering Science, University of Chinese Academy of Sciences, Beijing 100049, PR China

[3]Institute of Applied Physics and Computational Mathematics, Beijing 100094, PR China

(Received 23 May 2021; revised 5 March 2022; accepted 16 March 2022)

Helicity is a quadratic inviscid conservative quantity in three-dimensional turbulent flows and is crucial for turbulent system evolution. Helicity effects have mainly been highlighted over the past few decades to explore the intrinsic mechanism of turbulent flows, while the statistical characteristics of helicity itself are nearly absent in general anisotropic turbulent flows. In this paper, we investigate the helicity statistics in turbulent channel flows with streamwise rotation at moderate rotation numbers ($Ro_\tau = 7.5$, 15 and 30) and Reynolds numbers ($Re_\tau = 180$ and 395), including their spatial and scale distributions, anisotropy and cross-scale transfer. The appearance of a mean secondary flow in the spanwise direction corresponds to a mean streamwise vorticity, which indicates the presence of a high-helicity distribution. Numerical results reveal a regular helicity profile along the wall-normal direction, and a new peak is found in the near-wall region around $y^+ = 6$ of the streamwise or spanwise helicity profiles. The inter-scale helicity transfer is analysed by the filtering method, and the numerical consequences reveal that the second channel of the helicity cascade we proposed previously is dominant in contrast to the first channel. The rotation effects are explored by comparing the numerical results obtained under different rotation numbers. With increasing rotation number, more helical structures in the near-wall regions are present, with peaks of helicity profiles and fluxes coming closer to the wall. With a higher Reynolds number, their amplitudes are larger and scale-space transfer is strengthened. These systematic numerical analyses uncover the helicity distributions and transfer in wall-bounded turbulent flows.

Key words: turbulent boundary layers, rotating turbulence

1. Introduction

Rotating turbulent flows have been explored by theoretical derivation, numerical simulation and experiment for a long time, due to their potential value in the applications of

† Email addresses for correspondence: yan_zheng2021@163.com; lixl@imech.ac.cn

pumps, gas turbine blade passages and large-scale atmospheric and oceanic flows (Wu & Kasagi 2004; Weller & Oberlack 2006; Alkishriwi, Meinke & Schröder 2008). In contrast to homogeneous rotating turbulent flows (Pouquet & Mininni 2010) and turbulent channel flows with spanwise rotation (Yang & Wu 2012; Xia, Shi & Chen 2016), streamwise system rotation leads to a mean secondary flow in the spanwise direction, which is regarded as a unique characteristic (Bradshaw 1987). The mean spanwise secondary flow originates from the spanwise component of the Coriolis force, which appears in the governing equation of spanwise momentum (2.1*a*). The appearance of a mean secondary flow corresponds to a mean streamwise vorticity, which indicates the existence of high helicity in these wall-bounded turbulent flows (Oberlack *et al.* 2006; Masuda, Fukuda & Nagata 2008; Dai, Huang & Xu 2019). This motivates us to study helicity statistics based on our previous works of helicity in homogeneous and isotropic turbulent flows (Yan *et al.* 2020).

Previous studies of turbulent channel flow with streamwise rotation have mainly concentrated on mean secondary flows. Oberlack *et al.* (2006) carried out a Lie group analysis of the two-point correlation equations, and found that linear scaling laws of the mean streamwise velocity exist, which is confirmed by direct numerical simulations (DNS) and large-eddy simulations (LES). The experiments of turbulent channel flows with streamwise rotation were conducted through particle-image velocimetry (PIV) by Recktenwald *et al.* (2007), and the development of the mean secondary flows was observed. The statistical consequences of DNS and experiments are qualitatively similar, especially under the effect of the rotation rate. Later, Recktenwald, Alkishriwi & Schröder (2009) conducted LES with a larger spanwise computational domain, and obtained better agreement with PIV data. Helical wave decomposition was further developed by Yang, Su & Wu (2010), and was applied to viscous incompressible turbulent channel flows with streamwise rotation. They found that streamwise system rotation leads to polarity asymmetry, which motivates us to investigate helicity statistics in anisotropic turbulent flows. Yang & Wang (2018) performed DNS with moderate and high rotation numbers with sufficiently large streamwise computational domains to study the scales of the dynamics of Taylor–Görtler vortices, and Taylor–Görtler vortices can characterize the mean secondary flow according to instability analysis by Wall & Nagata (2006) and Masuda *et al.* (2008). DNS datasets were also used to investigate the effect of streamwise system rotation on pressure fluctuation, the self-constraint mechanism and the sustaining mechanism of Taylor–Görtler vortices (Yang *et al.* 2018, 2020*a*,*b*). Dai *et al.* (2019) studied the coherent structures in turbulent channel flows with streamwise system rotation through DNS and LES, and proposed that rotation promotes cyclones and suppresses anticyclones.

Helicity is a scalar product of velocity and vorticity, and it is one of the two quadratic inviscid invariants of three-dimensional flows (Moffatt & Tsinober 1992; Yan *et al.* 2019). It measures the degree of knottedness or linkage of vortex lines (Moffatt 1969), and the degree of broken symmetry (Betchov 1961). Seminal developments in helicity theory have been made in the past few decades, such as helicity cascade, scaling laws and their effects on energy cascade in homogeneous and isotropic turbulence (Brissaud 1973; Chen *et al.* 2003*b*; Biferale, Musacchio & Toschi 2012; Plunian *et al.* 2020). For helicity experiments, Scheeler *et al.* (2017) made a great breakthrough benefiting from high-resolution measuring techniques, and confirmed that helicity is a conservative variable even in viscous flows (Moffatt 2017). In our previous work (Yan *et al.* 2020), we proposed that there exist two channels of helicity cascade, and they can describe the inter-scale helicity transfer through different physical mechanisms, especially in anisotropic turbulent flows.

In anisotropic turbulent flows, there have been some valuable works focusing on the helicity effect on turbulent flow properties. Pelz *et al.* (1985) carried out DNS of plane Poiseuille and Taylor–Green vortex flows, and found that the velocity and vorticity tend to align in regions of low viscous dissipation. Correlations are not observed in Rogers & Moin (1987), except for low-dissipation regions near the outer edge of the buffer layer. Yokoi & Yoshizawa (1993) examined the helicity effects on swirling flows in a rotating frame and discussed the suppression of kinetic energy cascades through the inhomogeneity of helicity. Pieri *et al.* (2014) defined a new vector field, named cross-helicity, in a rotating frame and performed a high-resolution DNS of the developed homogeneous baroclinic turbulence. Nguyen & Papavassiliou (2020) used helicity to investigate scalar transport in wall-bounded turbulence through Lagrangian tracking and found that helicity levels are associated with the probability of markers remaining inside a coherent region. Hiejima (2020) studied the helicity effects on inviscid instability in Batchelor vortices, and proposed that helicity instability originates inside the vortex core. Povitsky (2017) proposed a three-dimensional flow in a cubic cavity driven by parallel walls with high helicity and found that mixing occurs faster than in the benchmark case.

However, there barely exists a detailed analysis of helicity itself for spatial distributions and inter-scale transfer in anisotropic turbulent flows, except for the helicity dynamics in Ekman boundary layers (Deusebio & Lindborg 2014). Hence, in this paper, we investigate the spatial distributions, multiscale distributions and inter-scale transfer of helicity in turbulent channel flows with streamwise rotation to reveal the helicity dynamics in wall-bounded turbulent flows and provide some theoretical suggestions for LES modelling.

The paper is organized as follows. In § 2, we introduce some computational details and mean statistics, to characterize the high helical status of turbulent channel flows with streamwise rotation. In § 3, the helicity dynamics is studied in detail, such as helicity profiles in different directions, helicity spectra and inter-scale helicity fluxes. The conclusions and discussions are presented in § 4.

2. Computational description and mean statistics

For incompressible turbulence, the Navier–Stokes equations in a rotating reference frame read as (Deusebio & Lindborg 2014; Vallis 2017)

$$\frac{\partial \boldsymbol{u}}{\partial t} + \boldsymbol{u}\cdot\nabla\boldsymbol{u} + 2\boldsymbol{\Omega}\times\boldsymbol{u} = -\nabla p + \nu\nabla^2\boldsymbol{u}, \tag{2.1a}$$

$$\nabla\cdot\boldsymbol{u} = 0, \tag{2.1b}$$

where $\boldsymbol{u}$ is the velocity vector in a rotating reference frame, p is the modified total pressure including the potential of the centrifugal force and ν is the kinematic viscosity. Here, $\boldsymbol{\Omega}$ is the rotating vector of the system, and $\boldsymbol{\Omega} = (\Omega_x, 0, 0)$. In our numerical simulations, Ω_x is set up to be a constant to satisfy the homogeneous rotation condition. We solved the above equations numerically in Cartesian coordinates with x, y and z directions, where x, y and z correspond to the streamwise, wall-normal and spanwise directions, respectively. Periodic boundary conditions are applied to the x and z directions, and we adopted no-slip and impermeable boundary conditions in the top and bottom walls along the y direction. Similar to the classical reference (Kim, Moin & Moser 1987), we employed the pseudospectral method. Fourier series are used to expand the velocity and vorticity in the streamwise and spanwise directions with uniform grids, and Chebyshev polynomials are employed in the wall-normal direction with Chebyshev–Gauss–Lobatto points. More computational details can be found in other valuable papers (Kim *et al.* 1987; Yang *et al.* 2010; Yang & Wang 2018).

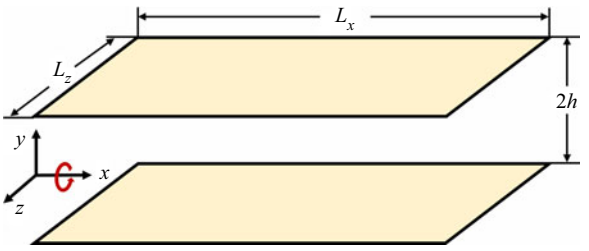

Figure 1. Sketch of turbulent channel flow with streamwise rotation.

2.1. *DNS with $Re_\tau = 180$ and 395 at moderate rotation numbers*

The presence of very long structures along the streamwise direction is one of the main characteristics of the present numerical simulations, and sufficiently long computational domains, especially in the streamwise direction, should be used to capture these long structures (Jiménez & Moin 1991; Wu & Kasagi 2004; Weller & Oberlack 2006; Recktenwald *et al.* 2007). Hence, at the present rotation numbers, we chose a largest computational domain with $128\pi \times 2 \times 8\pi$ in the streamwise, wall-normal and spanwise directions with $Ro_\tau = 30$ and $Re_\tau = 180$. Their definitions are $Ro_\tau = 2\Omega_x h/u_\tau$, $Re_\tau = hu_\tau/\nu$, and h is the half-channel height. The sketching diagram is shown in figure 1. In our numerical simulations, we use four rotation numbers of $Ro_\tau = 0, 7.5, 15$ and 30 with a fixed Reynolds number based on the wall-friction velocity $Re_\tau = 180$ to evaluate the rotation number effects, and compare the statistical consequences at a fixed rotation number $Ro_\tau = 7.5$ with $Re_\tau = 180$ and $Re_\tau = 395$ to evaluate the Reynolds number effects. The corresponding mesh setting of the DNS with $Re_\tau = 395$ at a weak streamwise rotation refers to Moser, Kim & Mansour (1999) with a small computational domain.

Similarly, the rotation number and Reynolds number based on the bulk velocity are obtained by

$$Ro_b = \frac{2\Omega_x h}{U_b}, \quad Re_b = \frac{hU_b}{\nu}. \tag{2.2a,b}$$

The bulk velocity is

$$U_b = \frac{1}{2h}\int_{-h}^{h} U(y)\,\mathrm{d}y. \tag{2.3}$$

The statistical analyses begin after the flows reach steady state, and we select the last $40h/u_\tau$ as the sampling time. Unless otherwise stated, all physical variables present in this paper are non-dimensionalized by the inner scale with the wall-friction velocity u_τ and the kinematic viscosity ν, and they are marked by superscript symbol $+$. Some characteristic parameters are listed in table 1.

We show the profiles of mean velocities in the streamwise and spanwise directions under different rotation numbers and Reynolds numbers in figure 2. Averaging is performed over the x–z plane and time, which is marked by $\langle\cdot\rangle$. The statistical results are consistent with previous work (Yang *et al.* 2010; Yang & Wang 2018), even though we adopted a larger Reynolds number. The inhibitory effects of the rotation number are reflected at the smaller mean streamwise velocity with higher rotation numbers. However, the statistical consequences of the mean spanwise velocity under different rotation numbers are slightly different from the results obtained in Yang *et al.* (2010). The rotation number effects on the mean spanwise velocity distribution are monotonic in the present numerical simulations. With the increase of rotation number, the amplitudes of the reverse flow in the core regions

Case	$L_x \times 2h \times L_z$	$N_x \times N_y \times N_z$	Re_b	Ro_b	Re_τ	Ro_τ
ST00	$32\pi \times 2 \times 8\pi$	$1024 \times 128 \times 512$	2783.76	0	180	0
ST07	$32\pi \times 2 \times 8\pi$	$1024 \times 128 \times 512$	2715.82	0.50	180	7.5
ST07R	$32\pi \times 2 \times 8\pi$	$4096 \times 192 \times 1536$	7893.19	0.38	395	7.5
ST15	$64\pi \times 2 \times 8\pi$	$2048 \times 128 \times 512$	2494.96	1.08	180	15
ST30	$128\pi \times 2 \times 8\pi$	$4096 \times 128 \times 512$	2181.43	2.48	180	30

Table 1. The computational configurations and some characteristic parameters of the flows.

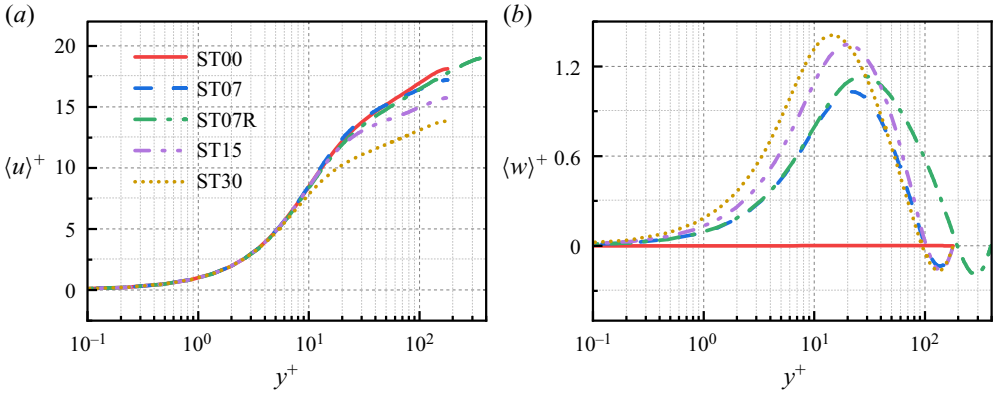

Figure 2. The profiles of mean velocities in the streamwise and spanwise directions.

are larger, and their peak locations are farther away from the channel centre. Likewise, the secondary flows close to the wall are also enhanced by higher rotation numbers. The Reynolds number effect is negligible in the near-wall regions, and the amplitudes of a mean secondary flow also increases with a higher Reynolds number. In contrast, there does not exist a secondary flow without rotation.

According to the homogeneity conditions in the streamwise and spanwise directions, the presence of a mean secondary flow leads to a non-zero-mean vorticity in the streamwise direction. Hence, the streamwise vorticity is also the main characteristic of turbulent channel flows with streamwise rotation. The profiles of mean vorticities in the streamwise $\langle\omega_x\rangle^+$ and spanwise directions $\langle\omega_z\rangle^+$ under different rotation numbers and Reynolds numbers are exhibited in figure 3. The mean wall-normal velocity and vorticity are zero, and we do not show their profiles in the current paper. In the present analysis, the mean streamwise vorticities are obtained by computing the slopes of the mean spanwise velocity vs wall-normal height y, and the mean spanwise vorticities are obtained by computing the slopes of the mean streamwise velocity vs wall-normal height y. For the mean streamwise vorticity in figure 3(a), there exists a peak within the half-channel. The peak is located around $y \approx \pm 0.8$, which is associated with the shoulder of the mean flows (Oberlack *et al.* 2006; Dai *et al.* 2019). The shoulder locations are easily affected by system rotation, and the amplitudes of the mean streamwise vorticities are enhanced by higher rotation numbers. In addition, the peak locations move closer towards the wall with the increase of rotation number. From the peak towards the wall or channel centre, the streamwise vorticity decreases monotonically. Around the wall, its sign is negative and its amplitude is very large, which is caused by large gradients of spanwise velocity within the near-wall regions. Meanwhile, around the channel centre, its sign is also negative and the cosine

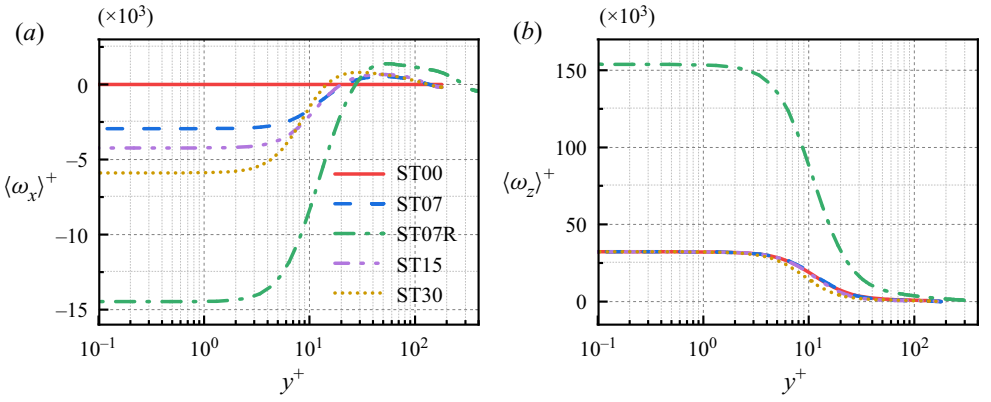

Figure 3. The profiles of mean vorticities in the streamwise and spanwise directions.

distribution is consistent with the inertial waves solution (Yang *et al.* 2010). The inhibitory effects of streamwise rotation are also reflected in the profiles of the mean spanwise vorticity in figure 3(*b*). With the increase of rotation number, the amplitudes of the mean spanwise vorticity are weakened, especially around the shoulder location. The large mean spanwise vorticity can be attributed to the large gradient of streamwise velocity within the boundary layers. As for Reynolds number effect, a higher Reynolds number corresponds to a more fully developed turbulent state, and it leads to larger vorticities at the wall boundary. However, the vorticity profiles at the streamwise and spanwise directions are similar at different Reynolds number.

2.2. *Numerical simulations with higher Reynolds numbers through DNS and LES*

The Reynolds number effects on the distributions of the mean secondary flows are worth exploring, and we carry out more numerical simulations with higher Reynolds numbers in this section. In order to be consistent with previous numerical settings, we adopted the LES method to investigate turbulent channel flows with $Ro_\tau = 7.5$ and $Re_\tau = 395$, 590 and 1000. The dynamic Smagorinsky model (Germano *et al.* 1991) is employed, and this model has been claimed to be successful for turbulent channel flows with streamwise rotation (Dai *et al.* 2019). In addition, DNS with a weak rotation number $Ro_\tau = 2$ and $Re_\tau = 1000$ and 2000 are also carried out to explore the Reynolds number effects. In order to decrease the computational cost, we select developed turbulent channel flows without any rotation as the initial flow fields. The raw dataset with $Re_\tau = 1000$ was downloaded from the Johns Hopkins Turbulence Database (JHTDB)(see http://turbulence.pha.jhu.edu) (Graham *et al.* 2016), and another raw dataset with $Re_\tau = 2000$ was downloaded from the website of the University of Texas at Austin (see https://turbulence.oden.utexas.edu/) (Hoyas & Jiménez 2006). The specific parameters including the computational domains, mesh cells, Reynolds numbers and rotation numbers are listed in table 2.

The mean streamwise and spanwise velocity profiles with the LES method are exhibited in figure 4, and the mean streamwise and spanwise velocity profiles with $Re_\tau = 395$ through the DNS method are compared to verify the success of the current LES model. For the streamwise velocity profile, the discrepancies are negligible except in the core regions with different Reynolds numbers. For the spanwise velocity profile, the mean secondary flows are preserved with different Reynolds numbers. The main difference lies

Case	$L_x \times 2h \times L_z$	$N_x \times N_y \times N_z$	Re_τ	Ro_τ	Method
ST07R395	$32\pi \times 2 \times 8\pi$	$1024 \times 96 \times 256$	395	7.5	LES
ST07R590	$32\pi \times 2 \times 8\pi$	$1536 \times 128 \times 512$	590	7.5	LES
ST07R1000	$32\pi \times 2 \times 8\pi$	$2048 \times 192 \times 1024$	1000	7.5	LES
JHU1000	$8\pi \times 2 \times 3\pi$	$1536 \times 512 \times 1024$	1000	2	DNS
UT2000	$8\pi \times 2 \times 3\pi$	$3072 \times 1024 \times 2048$	2000	2	DNS

Table 2. The computational settings and characteristic parameters of the flows with higher Reynolds numbers through DNS and LES.

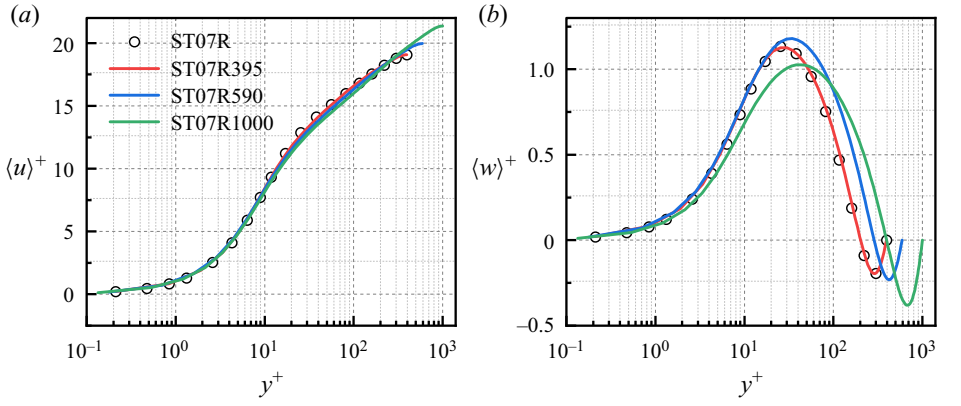

Figure 4. The profiles of mean velocities in the streamwise and spanwise directions with $Re_\tau = 395$, 590 and 1000. The mean streamwise and spanwise velocity profiles with $Re_\tau = 395$ are compared with symbol ○.

in the locations of peak and valley, and their locations move away from the wall with increasing the Reynolds number.

For the case with higher Reynolds number and a weak rotation number using the DNS method, we show the profiles of the mean streamwise and spanwise velocity profiles at different typical instants in figure 5 to investigate the effects of the presence of the streamwise rotation on the development process of the secondary flows. For the mean streamwise velocity profiles, the initial distributions are consistent with classical scaling laws with Re_τ = 1000 and 2000, and they assure us of the quality of the datasets we downloaded. With the presence of the streamwise rotation, the mean streamwise velocity profile begins to depart from the initial distributions. In the meanwhile, the mean spanwise velocity profile begins to develop, up to regular distributions of the secondary flows. With time, the system rotation drives a wall-normal transfer of spanwise momentum. The mean secondary flows begin to form within the near-wall regions, and then develop at the core regions. The development processes of the secondary flows are similar with Re_τ = 1000 and 2000, and eventually towards a stationary status. We highlight the presence of the mean secondary flows with high Reynolds numbers, and the statistical analysis of the stationary flow fields turns to the case with smaller Reynolds numbers and moderate rotation numbers.

The above statistical consequences reveal that the secondary flows are common at different Reynolds numbers, and the Reynolds number effects are mainly reflected in the locations of the peaks and valleys of the secondary flows. Nevertheless, the rotation number effects are the main factor for the secondary flows and are more complicated

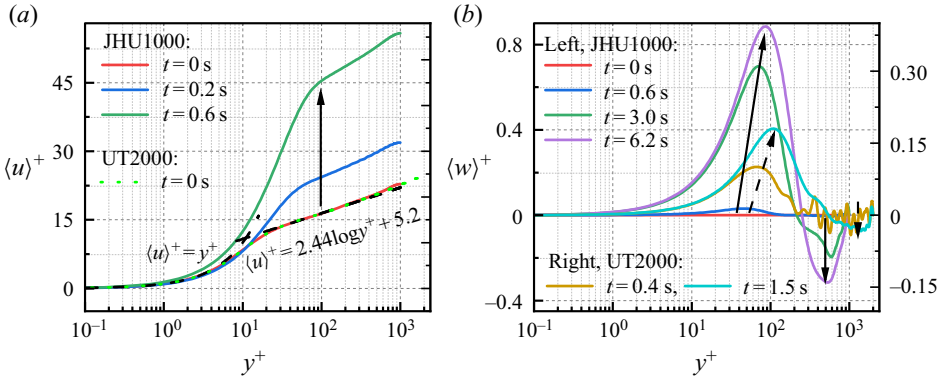

Figure 5. The profiles of mean velocities in the streamwise and spanwise directions at different typical instants with $Re_\tau = 1000$ and 2000.

(Yang *et al.* 2010; Yang & Wang 2018), and we select the cases with $Re_\tau = 180, 395$ at moderate rotation numbers to explore the helicity distributions and scale transfer in the following sections.

3. Helicity statistics

3.1. *Helicity profiles*

To further investigate the transfer paths of energy and helicity with background shear flows, we can decompose the fluid fields into mean and fluctuating components as $a = \langle a \rangle + a'$ (Härtel *et al.* 1994; Piomelli, Yu & Adrian 1996), and the fluctuating components can be further decomposed into resolved and unresolved components. In contrast to homogeneous and isotropic turbulence, new energy transfer paths exist for mean flows decomposed into resolved and unresolved components in wall-bounded turbulent flows. In this section, we show the mean and fluctuating components of energy and helicity to characterize the flow field. The resolved and unresolved components analysed by the filtering method are emphasized in a later section.

We can define the mean and fluctuating energy as

$$Em = \langle u \rangle^2 + \langle w \rangle^2, \quad Ef = u'^2 + v'^2 + w'^2. \tag{3.1a,b}$$

Similarly, the mean and fluctuating helicity can be defined as

$$Hm = Hxm + Hzm = \langle u \rangle \langle \omega_x \rangle + \langle w \rangle \langle \omega_z \rangle, \quad Hf = u'\omega_x' + v'\omega_y' + w'\omega_z'. \tag{3.2a,b}$$

Here, the prime $'$ denotes a fluctuating component. It should be mentioned that there exist another two components consisting of mean and fluctuating fields according to the Schwarz inequality. However, their ensemble averages are zero, and they are absent in the above decompositions.

The profiles of mean and fluctuating energy and helicity are shown in figure 6. The profiles of the mean energy are consistent with the distributions of streamwise velocity in figure 2. The main reason for this is that the streamwise velocity is dominant, even though there exists a mean secondary flow of the spanwise velocity. In the core regions, the amplitudes of the mean energy decrease with an increase of rotation number. However, the rotation effects on the fluctuating energy are different. With the presence of streamwise rotation, the fluctuating energy profiles are indeed changed, but rotation

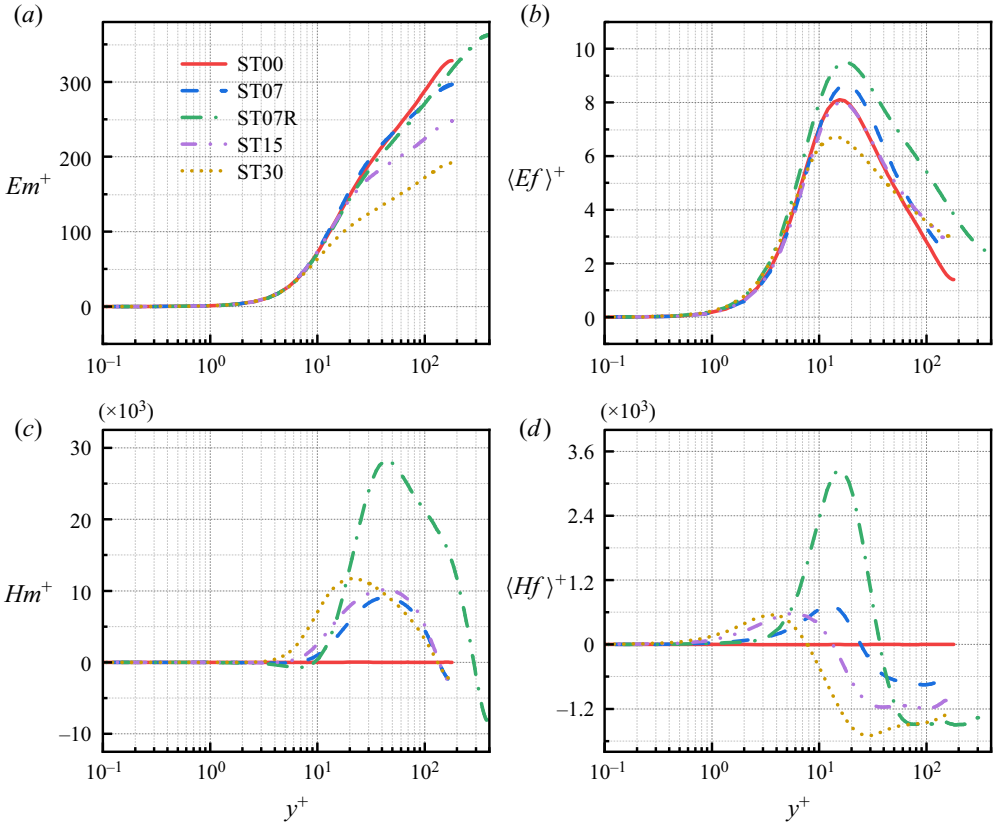

Figure 6. The profiles of the mean and fluctuating energy (*a*,*b*), and the mean and fluctuating helicity (*c*,*d*).

number effects are not monotonic in the near-wall regions. With the increase of rotation number in the core regions, the amplitudes of the fluctuating energy would increase. Hence, we can conclude that rotation would promote the energy path from the mean flows into fluctuating flows in the core regions. The Reynolds number effects on the fluctuating energy profiles are similar in the core regions. The mean and fluctuating helicity are nearly zero in turbulent channel flows without rotation, which verifies the necessity of exploring helicity statistics in turbulent channel flows with streamwise rotation. The profiles of the mean helicity in figure 6(*c*) indicate uniform helicity distributions of the main flows. With the increase of rotation number, the amplitudes of the mean helicity increase gradually in the core regions. In the near-wall regions, the amplitudes of helicity also increase with the increase of rotation number. Meanwhile, the peaks of the mean helicity distribution gradually approach the wall. The positive and negative helicities in different regions mainly depend on the mean spanwise velocity. We show the fluctuating helicity profiles at different rotation numbers in figure 6(*d*). The rotation effects are similar to those of the mean helicity. However, with a higher Reynolds number, the amplitudes of the mean and fluctuating components of helicity are larger with similar profile distributions, even at a weak rotation number. This means that high helicity might exist and be apparent in turbulent flows with high Reynolds numbers. In the present numerical simulations, the larger helicity profiles are obtained by relatively large streamwise rotations at relatively low Reynolds numbers, and the regulations might be

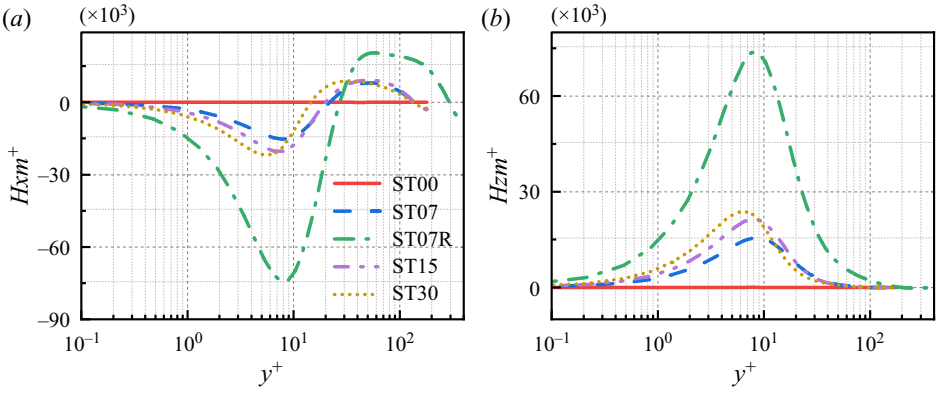

Figure 7. The profiles of the mean helicity in the streamwise direction (*a*) and the spanwise direction (*b*).

extended to natural or engineering turbulent flows with higher Reynolds numbers. The regular distributions pave the way for exploring the spectra and fluxes of helicity in later sections.

To investigate the helicity anisotropy in turbulent channel flows, we show the mean helicity profiles in the streamwise (Hx) and spanwise (Hz) directions in figure 7. Energy anisotropy has been explored in turbulent channel flows (del Alamo & Jiménez 2003; Dunn & Morrison 2003; Jiménez 2012), and we apply the methodology to helicity anisotropy. The mean wall-normal helicity is nearly zero, because the mean velocity and vorticity in the wall-normal direction are zero in turbulent channel flows, and we do not show their profiles for the sake of simplicity. Except for the peaks nearest to the wall, the profiles of the mean streamwise helicity are similar to the total helicity profiles in figure 6, both in terms of amplitudes and peak locations. However, new larger peaks of the mean streamwise and spanwise helicity exist around $y^+ = 6$ with $Ro_\tau = 30$. As for the cases with weak rotation, the peak locations may be larger, but all of them are smaller than the locations of the buffer layers. Their amplitudes are nearly the same, but their signs are different. Hence, the newly found peaks in the near-wall regions are not easily found in turbulent channel flows (Nguyen & Papavassiliou 2020). The presence of the new peaks can be attributed to the mean large vorticity in the near-wall regions. Dimensional analysis of the amplitudes of the mean streamwise velocity and vorticity, and the mean spanwise velocity and vorticity in the near-wall regions in figures 2 and 3, can also verify the relationship of the amplitudes of the mean streamwise and spanwise helicity. The newly found peaks indicate a high helical status in the near-wall regions, which also can be characterized by Taylor–Görtler-like vortices at the cross-section perpendicular to the streamwise direction in figure 8(*b*). In figure 8(*a*), the large-scale Taylor–Görtler vortices characterize the helical structures beyond the near-wall regions. The spiral characteristic represented by wall-normal and spanwise velocity vectors, accompanied by the mean streamwise velocity, reflects the three-dimensional helical structures.

3.2. *Helicity spectra*

The analysis of helicity anisotropy in the previous section indicates the necessity of studying the scale distributions of helicity in the streamwise and spanwise directions (Yang *et al.* 2020*b*). In figure 9, we display the one-dimensional premultiplied helicity spectra in the streamwise, wall-normal and spanwise directions depending on the wall

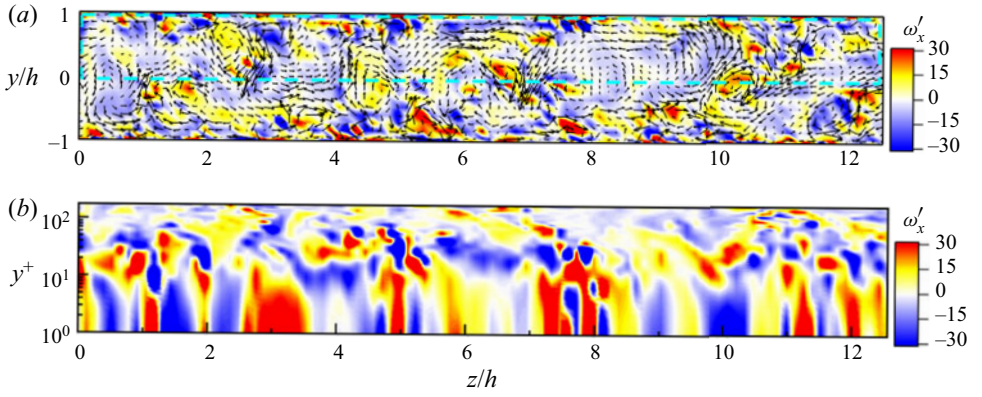

Figure 8. (*a*) Taylor–Görtler vortices visualized by the contours of the fluctuating streamwise vorticity and velocity vectors in the wall-normal and spanwise directions at the cross-section perpendicular to the streamwise direction in case ST07. (*b*) Contours of the fluctuating streamwise vorticity corresponding to the rectangular domains in (*a*), where we adopt a logarithmic vertical axis to present near-wall helical structures.

distance and the normalized streamwise wavelength $\lambda_x^+ = \lambda_x u_\tau/\nu$, where $\lambda_x = 2\pi/k_x$. The definition of the streamwise premultiplied helicity spectrum is

$$Hx = k_x\langle\hat{u}^*(k_x, y^+)\cdot\hat{\omega}_x(k_x, y^+)\rangle, \tag{3.3}$$

where k_x is the streamwise wavenumber, the asterisk denotes complex conjugate, $\hat{u}$ denotes the Fourier transform of the streamwise velocity and $\hat{\omega}_x$ denotes the Fourier transform of the streamwise vorticity. The definitions of the wall-normal and spanwise premultiplied helicity spectra are similar, and we do not show them for the sake of simplicity. According to the criteria proposed by Avsarkisov *et al.* (2014), Hoyas & Jiménez (2008) and Yang & Wang (2018), we select two isopleths for individual helicity spectra, and they are 62.5 % and 12.5 % of the individual positive and negative maximum amplitudes. The criteria are similar to those proposed by del Alamo *et al.* (2004) and Lozano-Durán & Jiménez (2014). In contrast to the energy spectra, the positive and negative helicities denote different chiralities, which complicates the helicity spectra. The log–log plots of helicity spectra emphasize the small scales of the helicity distribution in the near-wall regions. The helicity spectra in turbulent channel flows without rotation are chaotic, and we do not show them for the sake of simplicity. The peaks of the streamwise and spanwise helicity spectra are located around $y^+ = 6$, which are associated with the newly found peaks of the helicity profiles in figure 7. The locations of the peaks of the wall-normal helicity spectra are larger and mover close to the wall with an increase of rotation number. Streamwise helicity is negative in the near-wall regions and positive in the core regions, and this distribution regularity also applies to the wall-normal helicity spectra with weak rotation. However, the values of the streamwise helicity spectra are positive above the near-wall regions. With a larger rotation number, the positive distributions of the streamwise helicity spectra can be changed at different streamwise wavelengths. We can infer that the positive distributions of the streamwise helicity spectra might be absent with enough large rotation numbers. The development of the dominant role of the negative streamwise helicity spectra is associated with spatial transportation of the streamwise helicity along the wall-normal direction, and it can be evaluated by the general form of the classical Kolmogorov equation similar to the methodology of energy cascade in wall-bounded turbulent flows (Marati, Casciola & Piva 2004; Cimarelli *et al.* 2016).

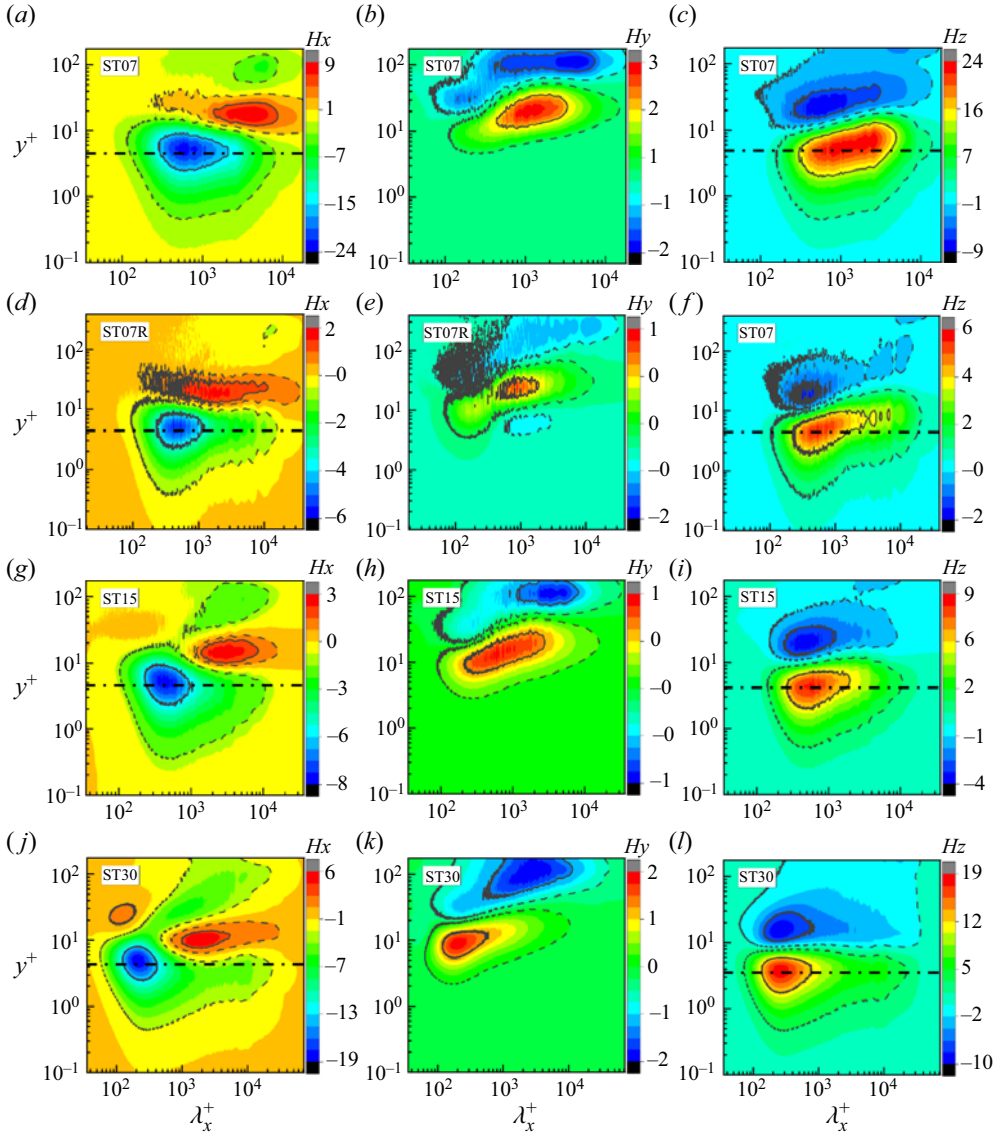

Figure 9. Premultiplied one-dimensional helicity spectra as functions of the streamwise wavelength and wall distance in the streamwise (*Hx*), wall-normal (*Hy*) and spanwise directions (*Hz*) at different rotation numbers and Reynolds numbers. The solid and dashed lines correspond to 62.5 % and 12.5 % of the individual positive and negative maximum amplitudes.

For wall-normal helicity spectra, the wavelengths of the peaks decrease gradually with an increase of rotation number. With a higher Reynolds number at a weak rotation, negative helicity spectra exist within the near-wall regions. According to the regulations of rotation number effects on the streamwise helicity spectrum distribution, we infer that the negative helicity spectra within the near-wall regions would disappear at a stronger rotation number. In the core regions with a higher Reynolds number or rotation number, most of wall-normal helicity spectra cannot be captured at the present resolution. The main reason lies in the propagation of inertial waves around the channel centre (Yang *et al.* 2010),

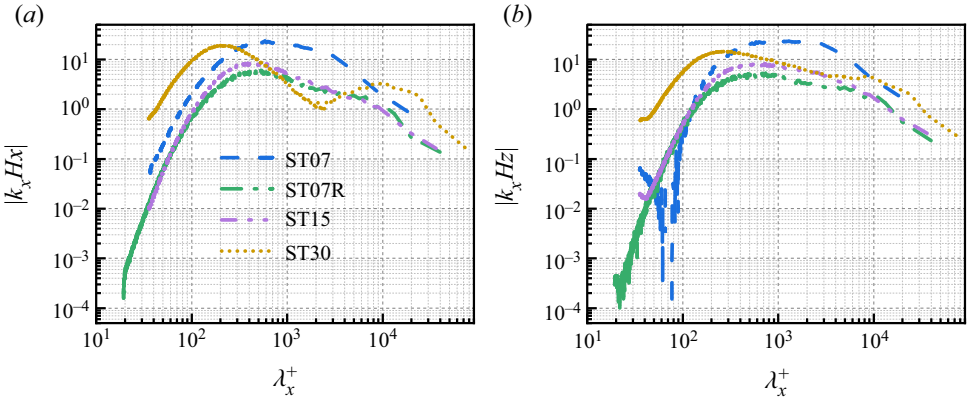

Figure 10. Premultiplied one-dimensional helicity spectra as functions of the streamwise wavelength, around the plane of $y^+ = 6$. The absolute values of the helicity spectra are selected for log–log plots.

which corresponds to an infinite streamwise computational domain. However, the present resolution can capture the high-helicity distributions in the near-wall regions and typical Taylor–Görtler vortices at $y/h = 0.5$ (Yang & Wang 2018).

The spanwise helicity spectra are rather regular, and two-layer distributions exist in the streamwise and wall-normal space. The first peak is also located around $y^+ = 6$, and it reflects a good correspondence with the streamwise spectra within the near-wall regions reflected in figure 7. The second peak is located above the buffer layers, and the interface is located around the buffer layers. The two-layer distributions of the spanwise helicity spectra are associated with two layers of streamwise-elongated roll cells (Yang & Wang 2018; Yang *et al.* 2020*b*). The counter-rotating Taylor–Görtler vortices weaken the velocity gradient in the buffer layer, and the energy sources are weakened correspondingly (Goto 2008). According to the scale-energy paths (Marati *et al.* 2004; Cimarelli *et al.* 2016), the energy source is located within the buffer layer, and transports to the viscous sublayer and log layer. The weakened energy source and spatial scale-energy transport by counter-rotating Taylor–Görtler vortices are consistent with previous conclusions of helicity effects on energy cascade (Alexakis 2017; Yan *et al.* 2020).

The scale distributions of helicity are shown in figure 10 around the plane of $y^+ = 6$. Apparent scale separations of helicity exist in three directions in the present numerical simulations with streamwise rotation, which highlights the complexity of near-wall turbulence from the perspective of helicity. The helicity spectra of the turbulent channel flows without rotation are disordered, and this reflects the multiscale nature of helicity under rotation effects. For streamwise helicity spectra, the rotation number effects are not monotonic. For spanwise helicity spectra, with the increase of rotation number, the small scales along the streamwise direction can obtain a fuller development, and the large-scale structures transfer to smaller scales. With a higher Reynolds number, more small scales can be resolved in figure 10. The helicity spectrum density in large scales is smaller in contrast to those with a low Reynolds number, and this means the transfer of helicity from large scales to small scales is strengthened with a high Reynolds number. However, two peaks of the streamwise and spanwise helicity spectra exist at a moderate rotation number. Consistent with the numerical consequences in figure 9, this phenomenon originates from the insufficient development of helicity at moderate rotation numbers. We infer that, with sufficiently high rotation numbers and Reynolds numbers, the characteristics of helicity in

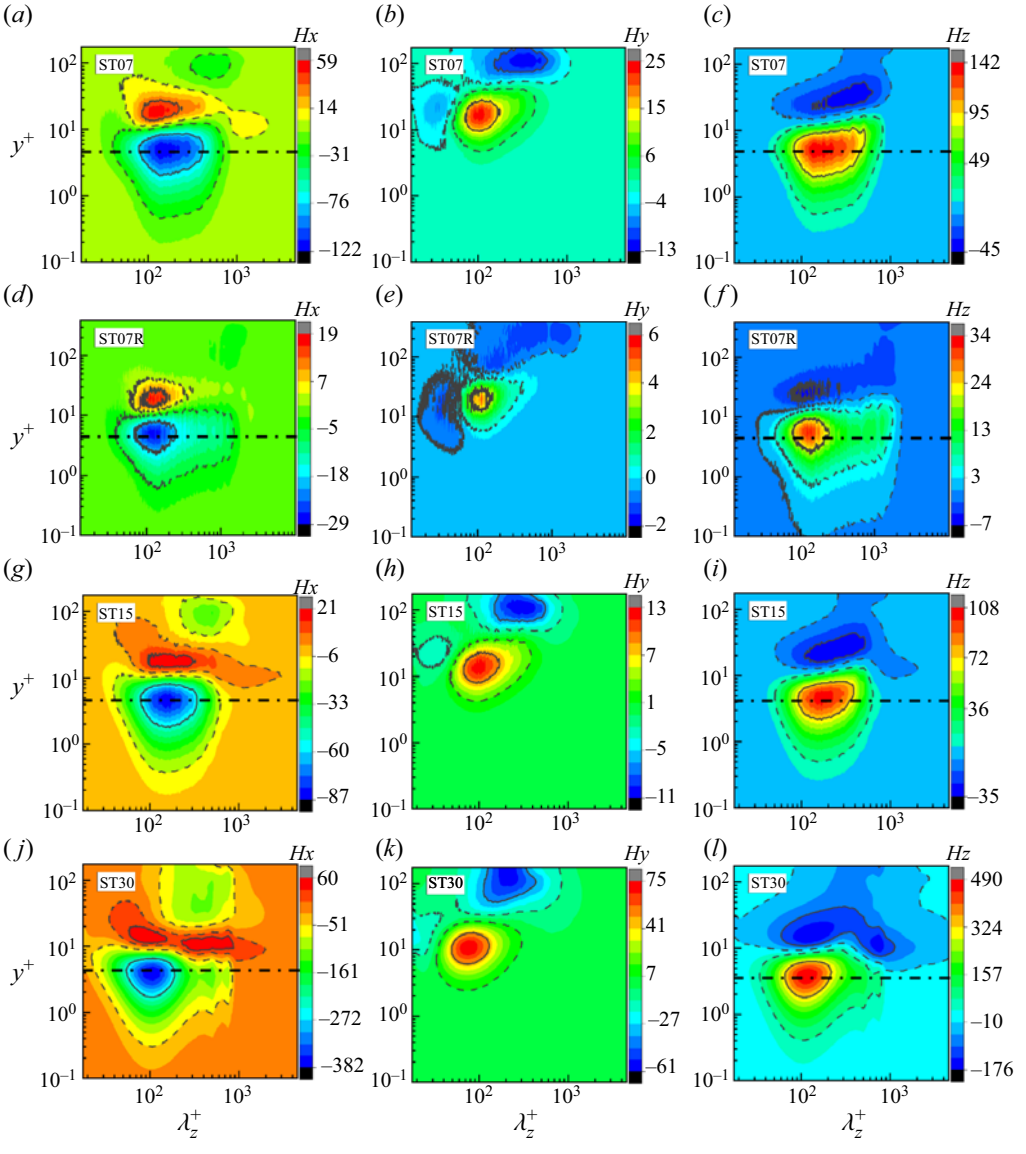

Figure 11. Premultiplied one-dimensional helicity spectra as functions of the spanwise wavelength and wall distance in the streamwise (*Hx*), wall-normal (*Hy*) and spanwise directions (*Hz*) at different rotation numbers. The solid and dash lines correspond to 62.5 % and 12.5 % of individual positive and negative maximum amplitudes.

homogeneous and isotropic turbulence (Brissaud 1973; Chen, Chen & Eyink 2003*a*; Yan *et al.* 2020) may appear. Hence, it has potential value to apply to some proven models to wall-bounded turbulence.

The premultiplied helicity spectra along the spanwise direction as functions of the normalized spanwise wavelength $\lambda_z^+ = \lambda_z u_\tau/\nu$, where $\lambda_z = 2\pi/k_z$, and wall distance are shown in figure 11. In contrast to streamwise scales, the spanwise scales are not sensitive to the rotation number, and the largest scales of the premultiplied helicity spectra of the spanwise scales can be easily resolved at the present numerical resolutions,

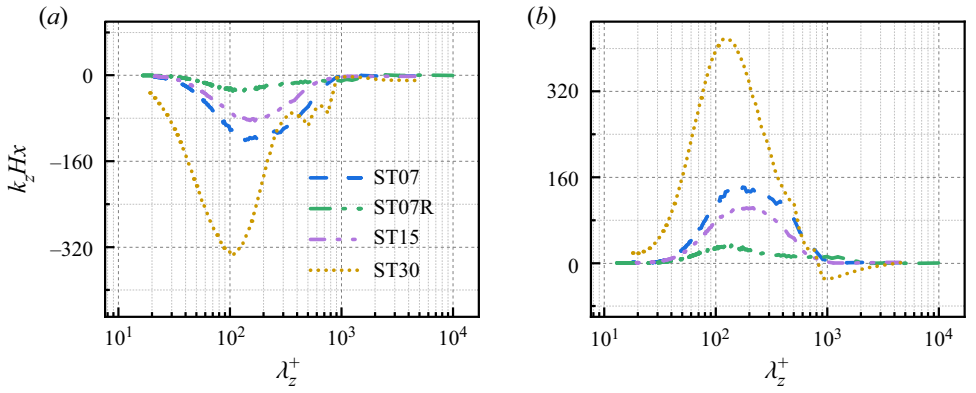

Figure 12. Premultiplied one-dimensional helicity spectra as functions of the spanwise wavelength, around the plane $y^+ = 6$.

especially in the near-wall regions. For streamwise helicity spectra, three apparent regions exist with the wall distance. In the near-wall regions of $y^+ < 10$, the helicity spectrum density is negative, and its amplitude is large enough to ensure a fully developed helicity cascade. The peak is also located around $y^+ = 6$, which is consistent with the near-wall peak appearing in the helicity profiles. In the logarithmic regions, the helicity spectrum density is positive, and its amplitude is smaller than that in the near-wall regions. In the core regions, the helicity spectrum density is also negative. The three-layer distribution of the streamwise helicity spectra reflects the complexity of the helicity statistics in wall-bounded turbulence. For wall-normal and spanwise helicity spectra, the helicity spectrum density is positive in near-wall regions and negative above the near-wall regions. For all premultiplied helicity spectra, the amplitudes gradually increase, and the peak location approaches the wall with the increase of rotation number. These regularities are similar to the premultiplied helicity spectra of the streamwise scales. With the increase of Reynolds number, the negative streamwise helicity would disappear, and the negative spanwise helicity distribution would be weakened. Similar to streamwise scales, the spatial fluxes of helicity along the wall-normal direction towards the wall are strengthened, and high-helicity distributions are present in the near-wall regions.

We exhibit the premultiplied helicity spectra of the spanwise scales around the plane of $y^+ = 6$ in figure 12. Apparent scale separations appear in all cases, reflecting the multiscale distributions of helicity in the near-wall regions. For all helicity spectra of the spanwise scales, the rotation number effects are not monotonic, and the amplitudes of helicity spectrum density at small scales decrease with the increase of rotation number at low rotation numbers. Hence, rotation effects on the helicity scale distributions hinder the transfer process of helicity from large scales to small scales. With a higher Reynolds number, the amplitudes of the streamwise and spanwise helicity spectrum densities are smaller, and the regulations are consistent with those of streamwise scales.

For all helicity spectra, the distribution of isolines reflects that the spanwise length scales of turbulent structures are smaller than the streamwise length scales. This indicates that the helical structures in the near-wall regions develop both in the streamwise and spanwise directions, and the streamwise lengths are larger than the spanwise lengths. This conclusion is consistent with previous work about energy distributions and Reynolds stress

scales (del Alamo & Jiménez 2003; Jiménez 2012). With the increase of rotation number, the amplitudes of the premultiplied helicity spectra increase overall.

In this section, we exhibited the premultiplied helicity spectra in the streamwise and spanwise directions. We find that the scale distributions of helicity are not chaotic, in contrast to the case without rotation, especially in the near-wall regions. The multiscale nature of helicity found in the near-wall regions highlights the complexity of wall-bounded turbulence, and we study the scale interactions of helicity in the near-wall regions in the next section.

3.3. *Helicity flux*

Based on the theoretical requirements of multiscale physics, the scale-to-scale fluxes of energy and helicity in three-dimensional turbulent flows are emphasized (Domaradzki *et al.* 1994; Piomelli *et al.* 1996). Yan *et al.* (2020) proposed that there exist two channels of helicity cascade for anisotropic turbulent flows. In this section, the two channels of the helicity cascade in turbulent channel flows with streamwise rotation are explored in detail by the filtering method.

The filtering operation for any variable $\boldsymbol{a}$ is defined by

$$\bar{\boldsymbol{a}}(\boldsymbol{x}, t) = \int \boldsymbol{G}(\boldsymbol{r}, \boldsymbol{x})\boldsymbol{a}(\boldsymbol{x} - \boldsymbol{r}, t)\,\mathrm{d}\boldsymbol{r}, \tag{3.4}$$

where $\boldsymbol{G}$ is the filter function, such as a box, Gaussian or sharp spectral filter (Pope 2001; Yan *et al.* 2019). Although discrepancies exist when adopting different filter functions (Buzzicotti *et al.* 2018), we employ the box filter function, which is moderate for capturing inverse energy cascades (Piomelli *et al.* 1991; Leslie & Quarini 1979). It is defined in one dimension as

$$\bar{a}_i = \frac{1}{4n}\left(a_{i-n} + 2\sum_{j=i-n+1}^{i+n-1} a_j + a_{i+n}\right), \tag{3.5}$$

where the filter width $\Delta = 2n\Delta x$, and Δx is the grid spacing (Martin, Piomelli & Candler 2000; Wang *et al.* 2012). In our numerical analysis, we apply the filter operation in the streamwise and spanwise directions. The energy flux can be defined as

$$\Pi_\Delta^E = -\tau_{ij}\bar{S}_{ij}, \tag{3.6}$$

where $\tau_{ij} = \overline{u_i u_j} - \bar{u}_i\bar{u}_j$ is the subgrid-scale stress, and $\bar{S}_{ij} = (1/2)(\partial\bar{u}_i/\partial x_j + \partial\bar{u}_j/\partial x_i)$ is the large-scale strain. Similar to the previous Reynolds decomposition, the energy flux can be rewritten as

$$\Pi_\Delta^E = \Pi_\Delta^{Em} + \Pi_\Delta^{Ef}, \tag{3.7}$$

where $\Pi_\Delta^{Em} = -\langle\tau_{ij}\rangle\langle\bar{S}_{ij}\rangle$ is the mean averaged in the streamwise and spanwise directions, $\Pi_\Delta^{Ef} = -(\tau_{ij} - \langle\tau_{ij}\rangle)(\bar{S}_{ij} - \langle\bar{S}_{ij}\rangle)$ is the fluctuating component (Härtel *et al.* 1994).

The mean and fluctuating components of energy flux have been investigated in previous works (Härtel *et al.* 1994; Härtel & Kleiser 1997, 1998), and the statistical consequences in figure 13 are consistent with these works. Here, we focus on the rotation effects on their amplitudes and distributions. For the mean component of the energy flux, their amplitudes are one order of magnitude larger than those of the fluctuating component, and the peak locations become closer to the wall with the increase of rotation number.

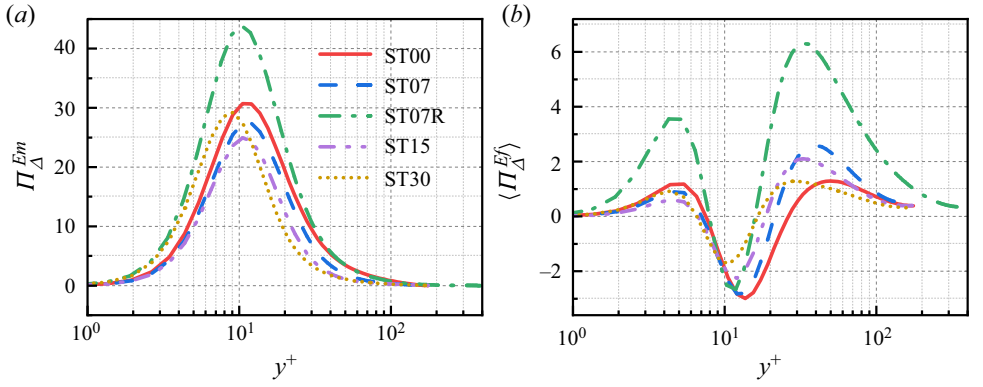

Figure 13. The mean and fluctuating components of energy flux at different rotation numbers. The filter width $\Delta = 8\Delta x$, where Δx is the streamwise grid spacing.

The self-amplification of the strain-rate field is the main contributor to the energy cascade (Carbone & Bragg 2020). Above the buffer layers ($y^+ > 10$), the rotation weakens the amplitudes of the mean energy flux. For the fluctuating component, the forward energy cascade is hindered, and the inverse energy cascade is promoted in the near-wall regions and hindered above the buffer layer. This hindered energy cascade may be associated with the helicity effect (Biferale *et al.* 2012; Alexakis 2017; Yan *et al.* 2020). With a higher Reynolds number, the mean and fluctuating components of the energy flux are larger, and the profile distributions are similar.

The helicity flux is defined as

$$\Pi_\Delta^H = \Pi_\Delta^{H1} + \Pi_\Delta^{H2}, \tag{3.8}$$

where Π_Δ^{H1} is the first channel of helicity cascade defined as $\Pi_\Delta^{H1} = -\tau_{ij}\bar{R}_{ij}$, and Π_Δ^{H2} is the second channel of helicity cascade defined as $\Pi_\Delta^{H2} = -\gamma_{ij}\bar{\Omega}_{ij}$. Here, $\bar{R}_{ij} = (1/2)(\partial\bar{\omega}_i/\partial x_j + \partial\bar{\omega}_j/\partial x_i)$ is the large-scale symmetric vorticity gradient, $\gamma_{ij} = (\overline{\omega_i u_j} - \bar{\omega}_i\bar{u}_j) - (\overline{\omega_j u_i} - \bar{\omega}_j\bar{u}_i)$ is the subgrid-scale vortex stretching stress and $\bar{\Omega}_{ij} = (1/2)(\partial\bar{u}_i/\partial x_j - \partial\bar{u}_j/\partial x_i)$ (Yan *et al.* 2020). Similarly, we can also decompose the helicity flux into mean and fluctuating components as

$$\Pi_\Delta^{H1} = \Pi_\Delta^{H1m} + \Pi_\Delta^{H1f}, \quad \Pi_\Delta^{H2} = \Pi_\Delta^{H2m} + \Pi_\Delta^{H2f}, \tag{3.9a,b}$$

$$\Pi_\Delta^{Hm} = \Pi_\Delta^{H1m} + \Pi_\Delta^{H2m}, \quad \Pi_\Delta^{Hf} = \Pi_\Delta^{H1f} + \Pi_\Delta^{H2f}. \tag{3.10a,b}$$

Here, $\Pi_\Delta^{H1m} = -\langle\tau_{ij}\rangle\langle\bar{R}_{ij}\rangle$ is the mean of the first-channel helicity flux, $\Pi_\Delta^{H1f} = -(\tau_{ij} - \langle\tau_{ij}\rangle)(\bar{R}_{ij} - \langle\bar{R}_{ij}\rangle)$ is the fluctuating component of the first-channel helicity flux, $\Pi_\Delta^{H2m} = -\langle\gamma_{ij}\rangle\langle\bar{\Omega}_{ij}\rangle$ is the mean of the second-channel helicity flux and $\Pi_\Delta^{H2f} = -(\gamma_{ij} - \langle\gamma_{ij}\rangle)(\bar{\Omega}_{ij} - \langle\bar{\Omega}_{ij}\rangle)$ is the fluctuating component of the second-channel helicity flux.

In figure 14, we show the mean and fluctuating components of helicity flux at different rotation numbers and Reynolds numbers. In contrast to the peaks located around $y^+ = 10$ of the energy flux in figure 13, the peaks of the helicity flux with a moderate rotation number are located around $y^+ = 6$, which is consistent with the distributions of the helicity spectra in the near-wall regions. The mean helicity flux in the case without rotation is nearly zero, which illustrates that the absence of the mean secondary flow results in zero-mean net flux of the helicity cascade. The rotation effects on the profiles of the mean

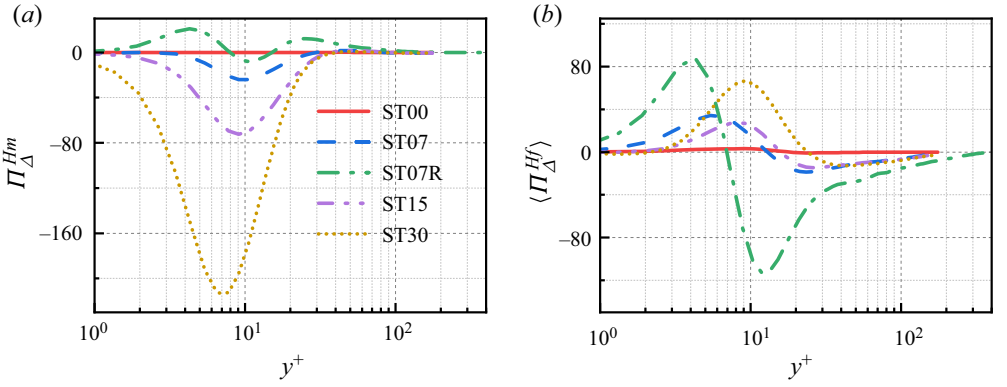

Figure 14. The mean and fluctuating components of helicity flux at different rotation numbers. The filter width $\Delta = 8\Delta x$.

helicity fluxes are similar to those of the helicity profiles and spectra. For the fluctuating component of the helicity flux, their amplitudes are comparable to the mean components, and the main reason for this lies in the large fluctuations of vorticity. Around the buffer layer, the fluctuating helicity cascade can be strengthened with an increase of the rotation number. It can be concluded that rotation intensifies the turbulent motions in the near-wall regions, and promotes helicity transfers from outer regions to near-wall regions.

Next, we compare the discrepancies in the two channels of the helicity cascade in figure 15. In our previous paper, we proposed that the first channel mainly originates from vortex twisting, and the second channel mainly originates from vortex stretching (Yan *et al.* 2020). In turbulent channel flows with streamwise rotation, there exists an apparent vortex twisting process induced both by rotation and advection. However, the vortex stretching process is still dominant because of the background shear flows. Hence, we infer that the second channel is dominant, and the effect of the first channel is not negligible in the present numerical simulations. The statistical results in figure 15 confirm our predictions. The amplitudes of the second channel are larger than those of the first channel, both for mean and fluctuating components. In addition, the peaks of the second channel also are located around $y^+ = 6$, and the peaks of the first channel are located above the buffer layers. In the near-wall regions, shear motions are dominant, and vortex stretching processes are also dominant, which leads to high helicity transfer through the second channel. While above the buffer layers, the vortex twisting processes gradually become important, which highlights the high helicity transfer through the first channel.

The spatial distributions of the first- and second-channel helicity fluxes are shown in figure 16 by three-dimensional isosurfaces. As we stated previously, the second channel of the helicity cascade mainly originates from the vortex stretching process, and the spatial distributions of the second channel present large-scale ordered streak structures. These ordered streaks are closely associated with Reynolds stress structures and high- and low-speed velocity streaks (Jiménez 2012). The ordered spatial distributions of the secondary channel indicate that the second channel is more intermittent than the first channel, which verifies the conclusions about intermittency discrepancy in homogeneous and isotropic turbulence (Yan *et al.* 2020). In contrast, the spatial distributions of the first channel are chaotic, and they present small-scale block structures, which is consistent with the vortex twisting process. The contours of the two channels in the insets of figure 16 indicate that the dominant spatial distributions of the second channel are concentrated

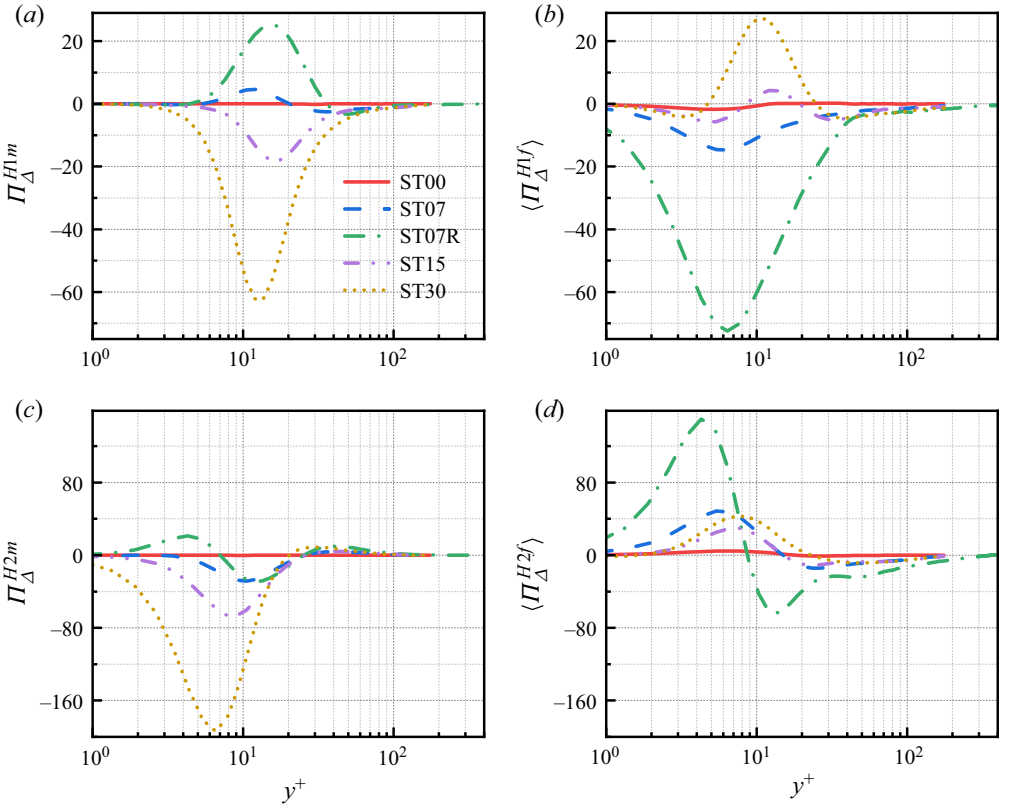

Figure 15. The mean and fluctuating components of the first- and second-channel helicity fluxes at different rotation numbers and Reynolds numbers. Here, $H1$ marks the first channel, and $H2$ marks the second channel. The filter width $\Delta = 8\Delta x$.

within the near-wall regions in contrast to the first channel, which results from a more dominant role of vortex stretching in the near-wall regions.

4. Conclusions and discussion

In this paper, we investigated the helicity statistics in turbulent channel flows with streamwise rotation, and focused on the profiles, spectra and scale-to-scale fluxes of helicity. More new physical phenomena were revealed in wall-bounded turbulent flows, in contrast to homogeneous and isotropic turbulence.

In contrast to turbulent channel flows without rotation, the helicity profiles of turbulent channel flows with streamwise rotation are regular along the wall-normal direction. The appearance of high helicity mainly originates from the mean secondary flows, and it manifests as the mean spanwise velocity and streamwise vorticity. The sign of the helicity is positive in the near-wall regions and negative in the core regions, and its amplitude changes continuously with the wall distance. Helicity anisotropy reflects on the different distributions in the streamwise, wall-normal and spanwise directions, and new peaks of the mean streamwise and spanwise helicity profiles exist in the near-wall regions around $y^+ = 6$. These peaks are located under the buffer layers, and they differ with the turbulent energy distribution. The near-wall peaks are concealed in the total helicity profiles, because their amplitudes are nearly the same, and their signs are opposite.

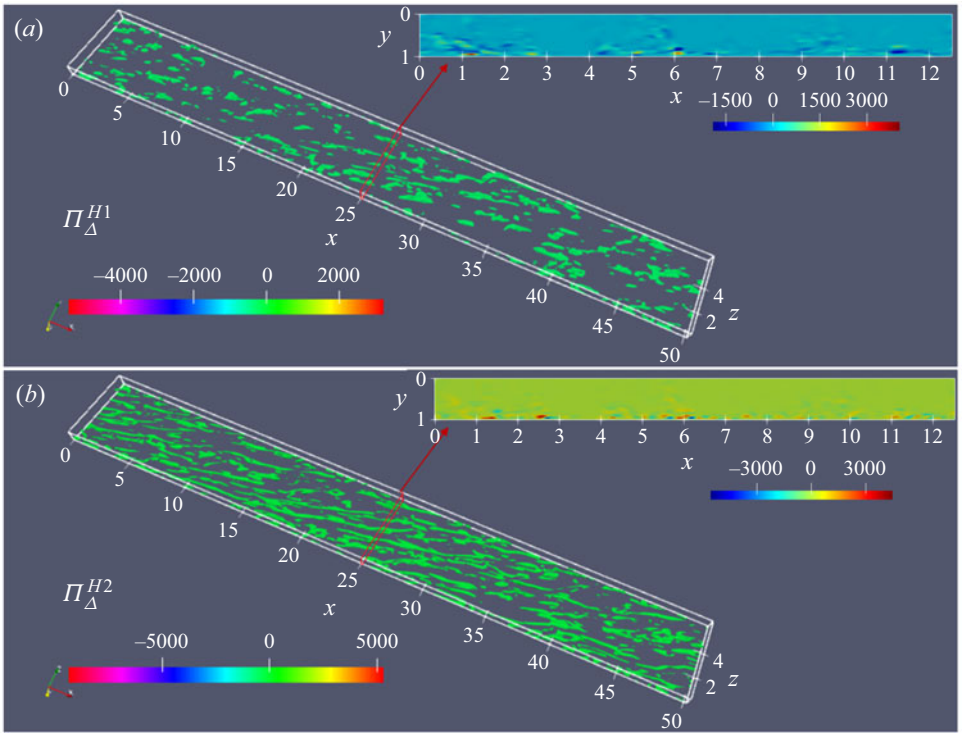

Figure 16. Isosurfaces of the first channel (*a*) and second channel (*b*) of helicity cascade with filter width $\Delta = 8\Delta x$ in case ST07. The thresholds are selected as 10 % of the corresponding maximum. The insets are the corresponding contours of a cross-section perpendicular to the streamwise direction.

With the increase of rotation number, all peak locations of the helicity profiles move closer to the wall. Rotation promotes helicity spatial transfer from outer regions to near-wall regions, and it presents highly helical structures in the near-wall regions. Reynolds number effects are similar to rotation effects. With a higher Reynolds number, the developments of turbulent flows are fuller, which is represented as the stronger nonlinearity, the more small scales resolved, the larger amplitudes of energy and helicity and the stronger cross-scale transfer. Even at a weak rotation, the helicity distributions tend to be regular at a higher Reynolds number.

The positive and negative signs of the helicity render complex its spatial and scale distributions in wall-bounded turbulence. The high helicity amplitudes in the near-wall regions indicate that multiscale developments of helicity may exist. The apparent scale separations of premultiplied helicity spectra confirm this prediction, and we found that multilayer helicity distributions also exist along the wall-normal direction. Rotation promotes the small-scale development of helicity, especially in the near-wall regions. The premultiplied helicity spectra of the streamwise and spanwise scales illustrate that highly helical structures develop both in the streamwise and spanwise directions, and the streamwise scales are larger than the spanwise scales.

We adopted filtering and Reynolds decomposition methods to investigate the dual channels of the helicity cascade we proposed previously (Yan *et al.* 2020). The high shearing motions occurring in the near-wall regions mean that the vortex stretching is dominant in contrast to vortex twisting. Hence, the second channel is dominant for

the helicity cascade. In addition, the peaks of the helicity cascade through the second channel are also located around $y^+ = 6$, and they are closely associated with the peaks of streamwise or spanwise helicity profiles. The spatial distributions of the second channel are ordered, and their scales are very large along the streamwise direction. Its distributions are similar to the Reynolds stress or streak structures, and are more intermittent than in the first channel.

The high and regular helicity distribution in the wall-bounded turbulent flows provides an alternative representation for the secondary flows, which are associated with the presence of non-zero streamwise vorticity (Bradshaw 1987). According to the origin discrepancy, there are first and second kinds of Prandtl's secondary flow. The first kind originates from the imbalance between the cross-stream pressure gradient and centrifugal force, such as occurs in curved pipes (Berger, Talbot & Yao 1983; Hüttl & Friedrich 2001; Noorani, El Khoury & Schlatter 2013; Chin *et al.* 2020). The second kind originates from Reynolds stress gradients with non-circular cross-section, such as occurs in duct flows (Modesti *et al.* 2018; Pirozzoli *et al.* 2018; Orlandi & Pirozzoli 2020). The presence of the streamwise vorticity combined with the streamwise velocity corresponds to a high and regular helicity distribution. We may infer that the high and regular helicity distribution is general in secondary flows. More structure information of the secondary flows can be uncovered via investigating the statistical characteristics of helicity. In the Appendix, we select the turbulent duct flows with different Reynolds numbers (second kind of Prandtl's secondary flow) to illustrate the similarity and discrepancy of the helicity distribution between turbulent duct flows and turbulent channel flows with streamwise rotation. It can be concluded that the high and regular helicity distribution is general in secondary flows, and this phenomenon is insensitive to the Reynolds number, especially within the near-wall regions.

The discovery of the new peaks in the near-wall regions uncovers the helicity distributions, and it provides a theoretical foundation to confirm helicity effects in wall-bounded turbulent flows. In the future, larger computational domains with higher rotation numbers should be investigated to verify the nonmonotonic rotation effects. More anisotropic turbulent flows can be selected to investigate their helicity statistics, such as pipe flows with rotation, Rayleigh–Taylor instabilities, etc.

Acknowledgements. The authors thank the J. Hopkins turbulence database and the university of Texas at Austin for providing public turbulent channel flow datasets, and Professor S. Pirozzoli1 and Professor D. Modesti for sharing their square duct flows. The authors also thank National Supercomputer Center in Tianjin (NSCC-TJ) and National Supercomputer Center in GuangZhou (NSCC-GZ) for providing computer time. In addition, we would like to express our honest appreciation to Professor Y. Zixuan for his generosity in providing in-house numerical simulation codes.

Funding. This work was supported by the National Key Research and Development Program of China (2019YFA0405300 and 2020YFA0711800), and the National Natural Science Foundation of China (NSFC grant nos 12072349 and 91852203).

Declaration of interests. The authors report no conflict of interest.

Author ORCIDs.
Changping Yu https://orcid.org/0000-0002-2126-1344;
Running Hu https://orcid.org/0000-0002-3423-5583;
Zheng Yan https://orcid.org/0000-0002-8813-3216.

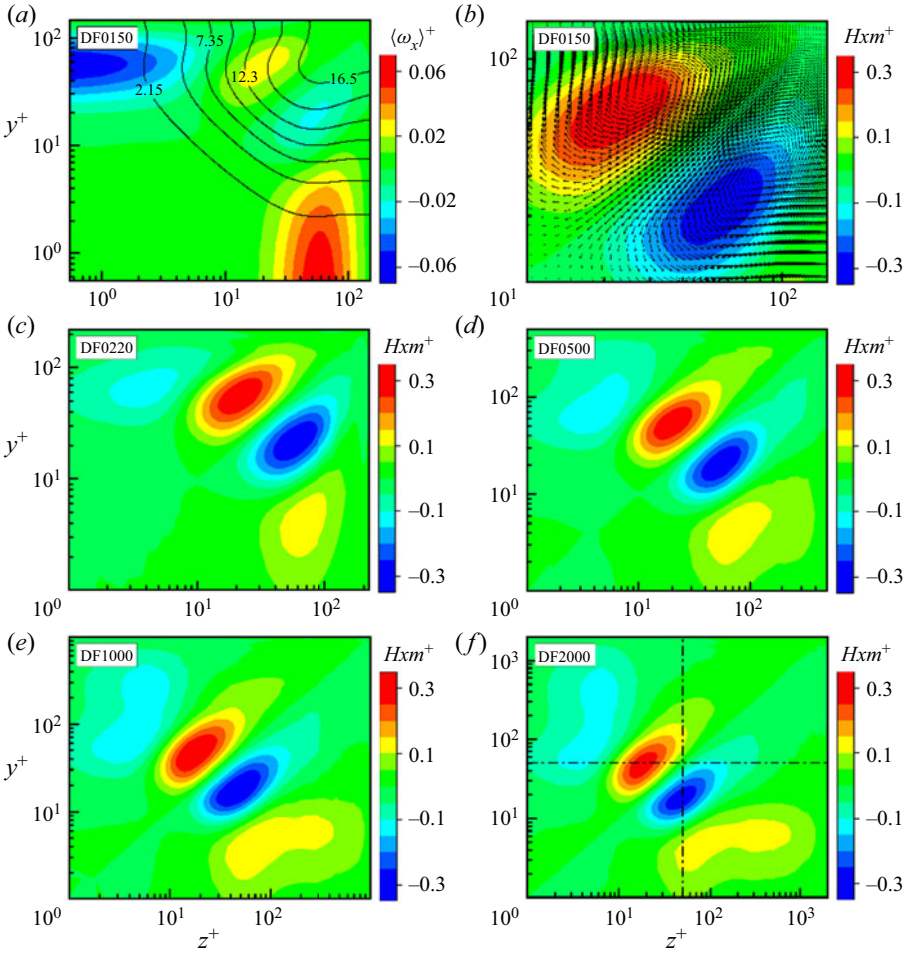

Figure 17. (*a*) Cross-section contour of the normalized mean streamwise vorticity, accompanied by the isolines of the normalized mean streamwise velocity with $Re_\tau = 150$. (*b*) Cross-section contour of the normalized mean streamwise helicity, accompanied by the vectors of the normalized mean wall-normal velocities with $Re_\tau = 150$. Cross-section contours of the normalized mean streamwise helicity with $Re_\tau = 220$ (*c*), $Re_\tau = 500$ (*d*), $Re_\tau = 1000$ (*e*) and with $Re_\tau = 2000$ (*f*). The two dot-dashed lines mark the positions analysed subsequently.

Appendix. Helicity distribution in square duct flows

In this section, we select square duct flows as one type of Prandtl's secondary flow of the second kind, to show the helicity distribution in other wall-bounded turbulent flows. The cross-section flow statistics were downloaded from a public turbulent database (see http://newton.dma.uniroma1.it/square_duct/), including the mean streamwise velocity $\langle u\rangle$, the mean streamwise vorticity $\langle\omega_x\rangle$ and the mean wall-normal velocities $\langle v\rangle$ and $\langle w\rangle$, with $Re_\tau = 150, 220, 500, 1000$ and 2000. This public turbulent database is highly credible, and has been validated in previous valuable works (Pirozzoli *et al.* 2018; Modesti *et al.* 2018; Orlandi & Pirozzoli 2020).

We show the numerical results of the turbulent duct flows in figure 17, and all variables are non-dimensionalized by the inner scale. Only a quarter slice is selected for the sake of simplicity. The mean streamwise vorticity contour and bended isolines of the mean streamwise velocity in figure 17(*a*) reflect the eight counter-rotating eddies in turbulent

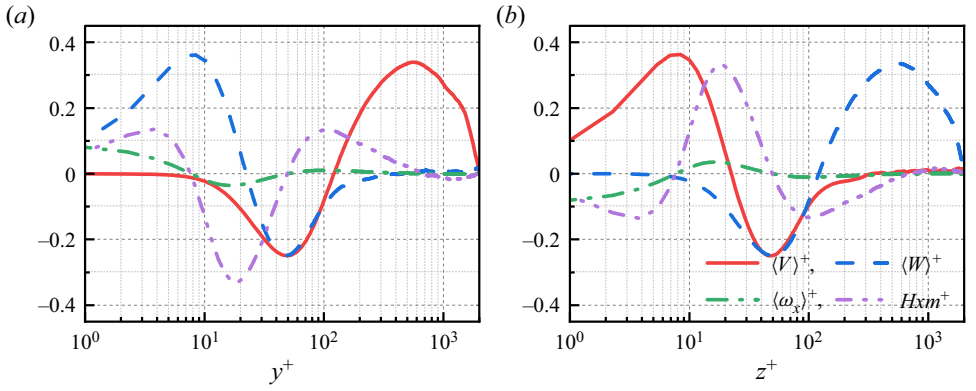

Figure 18. The normalized mean wall-normal velocities $\langle v\rangle^+$ and $\langle w\rangle^+$, the normalized mean streamwise vorticity and the normalized mean streamwise helicity profiles (a) with $z^+ \approx 50$ and (b) with $y^+ \approx 50$.

duct flows, which bring high-momentum fluid from the duct towards the corners (Pirozzoli *et al.* 2018). In addition, there are also corresponding counter-rotating eddies within the near-wall regions, which are visual in the current log–log coordinates. The counter-rotating eddies outside the near-wall regions can also be represented by regular streamwise helicity distribution, which applies to all current cases with different Reynolds numbers. This means that the secondary flows in turbulent duct flows represented by a regular distribution might be general. With the increase of Reynolds number, the mean streamwise helicity increases slightly, and its peak locations tend to approach the corners. This Reynolds number effect is similar with that in turbulent channel flows with streamwise rotation.

The profile distributions associated with the secondary flows marked in figure 17(f) are exhibited in figure 18. In contrast to the turbulent channel flows with streamwise rotation, the secondary flows exist both in two directions within the cross-section. Hence, the secondary flow profiles apply to both wall-normal velocities $\langle v\rangle^+$ and $\langle w\rangle^+$. The profile distributions of $\langle v\rangle^+$ and $\langle w\rangle^+$ are on the diagonal symmetry in figures 18(a) and 18(b), respectively. The diagonal symmetry determines that the normalized mean streamwise vorticities in figures 18(a) and 18(b) are opposite numbers. The mean streamwise helicity profile distribution is a combined result of the mean streamwise velocity and vorticity. The mean streamwise velocity increase with the increase of the wall distance, while the mean streamwise vorticity is largest within the near-wall regions. Hence, the high-helicity distribution appears around the middle regions. The numerical consequences with $Re_\tau = 2000$ in figures 18(a) and 18(b) indicate that the high helicity is locate around $y^+ = z^+ \approx 20$. The high-helicity distribution regulation also applies to the cases with other lower Reynolds numbers, and this means that the helicity distribution is insensitive to Reynolds number.

References

DEL ALAMO, J.C. & JIMÉNEZ, J. 2003 Spectra of the very large anisotropic scales in turbulent channels. *Phys. Fluids* **15**, L41–L44.

DEL ALAMO, J.C., JIMÉNEZ, J., ZANDONADE, P. & MOSER, R.D. 2004 Scaling of the energy spectra of turbulent channels. *J. Fluid Mech.* **500**, 135–144.

ALEXAKIS, A. 2017 Helically decomposed turbulence. *J. Fluid Mech.* **812**, 752–770.

ALKISHRIWI, N., MEINKE, M. & SCHRÖDER, W. 2008 Large-eddy simulation of streamwise-rotating turbulent channel flow. *Comput. Fluids* **37**, 786–792.

AVSARKISOV, V., CALVO, S.H., OBERLACK, M. & GARCÍA-GALACHE, J.P. 2014 Turbulent plane Couette flow at moderately high Reynolds number. *J. Fluid Mech.* **751**, R1.
BERGER, S.A., TALBOT, L. & YAO, L.S. 1983 Flow in curved pipes. *Annu. Rev. Fluid Mech.* **15**, 461–512.
BETCHOV, R. 1961 Semi-isotropic turbulence and helicoidal flows. *Phys. Fluids* **4**, 925–926.
BIFERALE, L., MUSACCHIO, S. & TOSCHI, F. 2012 Inverse energy cascade in three-dimensional isotropic turbulence. *Phys. Rev. Lett.* **108**, 164501.
BRADSHAW, P. 1987 Turbulent secondary flows. *Annu. Rev. Fluid Mech.* **19**, 53–74.
BRISSAUD, A. 1973 Helicity cascades in fully developed isotropic turbulence. *Phys. Fluids* **16**, 1366–1367.
BUZZICOTTI, M., LINKMANN, M., ALUIE, H., BIFERALE, L., BRASSEUR, J. & MENEVEAU, C. 2018 Effect of filter type on the statistics of energy transfer between resolved and subfilter scales from a-priori analysis of direct numerical simulations of isotropic turbulence. *J. Turbul.* **19**, 167–197.
CARBONE, M. & BRAGG, A.D. 2020 Is vortex stretching the main cause of the turbulent energy cascade? *J. Fluid Mech.* **883**, R2.
CHEN, Q.N., CHEN, S.Y. & EYINK, G.L. 2003*a* The joint cascade of energy and helicity in three-dimensional turbulence. *Phys. Fluids* **15**, 361–374.
CHEN, Q.N., CHEN, S.Y., EYINK, G.L. & HOLM, D.D. 2003*b* Intermittency in the joint cascade of energy and helicity. *Phys. Rev. Lett.* **90**, 214503.
CHIN, R.C., VINUESA, R., ÖRLÜ, R., CARDESA, J.I., NOORANI, A., CHONG, M.S. & SCHLATTER, P. 2020 Backflow events under the effect of secondary flow of Prandtl's first kind. *Phys. Rev. Fluids* **5**, 074606.
CIMARELLI, A., DE ANGELIS, E., JIMÉNEZ, J. & CASCIOLA, C.M. 2016 Cascades and wall-normal fluxes in turbulent channel flows. *J. Fluid Mech.* **796**, 417–436.
DAI, Y.J., HUANG, W.X. & XU, C.X. 2019 Coherent structures in streamwise rotating channel flow. *Phys. Fluids* **31**, 021204.
DEUSEBIO, E. & LINDBORG, E. 2014 Helicity in the Ekman boundary layer. *J. Fluid Mech.* **755**, 654–671.
DOMARADZKI, J.A., LIU, W., HÄRTEL, C. & KLEISER, L. 1994 Energy transfer in numerically simulated wall-bounded turbulent flows. *Phys. Fluids* **6**, 1583–1599.
DUNN, D.C. & MORRISON, J.F. 2003 Anisotropy and energy flux in wall turbulence. *J. Fluid Mech.* **491**, 353–378.
GERMANO, M., PIOMELLI, U., MOIN, P. & CABOT, W.H. 1991 A dynamic subgrid-scale eddy viscosity model. *Phys. Fluids* A **3**, 1760–1765.
GOTO, S. 2008 A physical mechanism of the energy cascade in homogeneous isotropic turbulence. *J. Fluid Mech.* **605**, 355–366.
GRAHAM, J., *et al.* 2016 A web services accessible database of turbulent channel flow and its use for testing a new integral wall model for LES. *J. Turbul.* **17**, 181–215.
HÄRTEL, C. & KLEISER, L. 1997 Galilean invariance and filtering dependence of near-wall grid-scale/subgrid-scale interactions in large-eddy simulation. *Phys. Fluids* **9**, 473–475.
HÄRTEL, C. & KLEISER, L. 1998 Analysis and modelling of subgrid-scale motions in near-wall turbulence. *J. Fluid Mech.* **356**, 327–352.
HÄRTEL, C., KLEISER, L., UNGER, F. & FRIEDRICH, R. 1994 Subgrid-scale energy transfer in the near-wall region of turbulent flows. *Phys. Fluids* **6**, 3130–3143.
HIEJIMA, T. 2020 Helicity effects on inviscid instability in Batchelor vortices. *J. Fluid Mech.* **897**, A37.
HOYAS, S. & JIMÉNEZ, J. 2006 Scaling of the velocity fluctuations in turbulent channels up to $Re_\tau = 2003$. *Phys. Fluids* **18**, 011702.
HOYAS, S. & JIMÉNEZ, J. 2008 Reynolds number effects on the Reynolds-stress budgets in turbulent channels. *Phys. Fluids* **20**, 101511.
HÜTTL, T.J. & FRIEDRICH, R. 2001 Direct numerical simulation of turbulent flows in curved and helically coiled pipes. *Comput. Fluids* **30**, 591–605.
JIMÉNEZ, J. 2012 Cascades in wall-bounded turbulence. *Annu. Rev. Fluid Mech.* **44**, 27–45.
JIMÉNEZ, J. & MOIN, P. 1991 The minimal flow unit in near-wall turbulence. *J. Fluid Mech.* **225**, 213–240.
KIM, J., MOIN, P. & MOSER, R. 1987 Turbulence statistics in fully developed channel flow at low Reynolds number. *J. Fluid Mech.* **177**, 133–166.
LESLIE, D.C. & QUARINI, G.L. 1979 The application of turbulence theory to the formulation of subgrid modelling procedures. *J. Fluid Mech.* **91**, 65–91.
LOZANO-DURÁN, A. & JIMÉNEZ, J. 2014 Effect of the computational domain on direct simulations of turbulent channels up to $Re_\tau = 4200$. *Phys. Fluids* **26**, 011702.
MARATI, N., CASCIOLA, C.M. & PIVA, R. 2004 Energy cascade and spatial fluxes in wall turbulence. *J. Fluid Mech.* **521**, 191–215.
MARTIN, M.P., PIOMELLI, U. & CANDLER, G.V. 2000 Subgrid-scale models for compressible large-eddy simulations. *Theor. Comput. Fluid Dyn.* **13**, 361–376.

MASUDA, S., FUKUDA, S. & NAGATA, M. 2008 Instabilities of plane Poiseuille flow with a streamwise system rotation. *J. Fluid Mech.* **603**, 189–206.
MODESTI, D., PIROZZOLI, S., ORLANDI, P. & GRASSO, F. 2018 On the role of secondary motions in turbulent square duct flow. *J. Fluid Mech.* **847**, R1.
MOFFATT, H.K. 1969 Degree of knottedness of tangled vortex lines. *J. Fluid Mech.* **35**, 117–129.
MOFFATT, H.K. 2017 Helicity-invariant even in a viscous fluid. *Science* **357**, 448–449.
MOFFATT, H.K. & TSINOBER, A. 1992 Helicity in laminar and turbulence flow. *Annu. Rev. Fluid Mech.* **24**, 281–312.
MOSER, R.D., KIM, J. & MANSOUR, N.N. 1999 Direct numerical simulation of turbulent channel flow up to $Re_\tau = 590$. *Phys. Fluids* **11**, 943–945.
NGUYEN, Q. & PAPAVASSILIOU, D.V. 2020 Using helicity to investigate scalar transport in wall turbulence. *Phys. Rev. Fluids* **5**, 062601.
NOORANI, A., EL KHOURY, G.K. & SCHLATTER, P. 2013 Evolution of turbulence characteristics from straight to curved pipes. *Intl J. Heat Fluid Flow* **41**, 16–26.
OBERLACK, M., CABOT, W., REIF, B.A.P. & WELLER, T. 2006 Group analysis, direct numerical simulation and modelling of a turbulent channel flow with streamwise rotation. *J. Fluid Mech.* **562**, 383–403.
ORLANDI, P. & PIROZZOLI, S. 2020 Turbulent flows in square ducts: physical insight and suggestions for turbulence modellers. *J. Turbul.* **21**, 1–25.
PELZ, R.B., YAKHOT, V., ORSZAG, S.A., SHTILMAN, L. & LEVICH, E. 1985 Velocity-vorticity patterns in turbulent flow. *Phys. Rev. Lett.* **54**, 2505–2508.
PIERI, A.B., GODEFERD, F.S., CAMBON, C., DUBRULLE, B. & THALABARD, S. 2014 Cross-helicity in rotating homogeneous shear-stratified turbulence. *Phys. Rev. Lett.* **112**, 114501.
PIOMELLI, U., CABOT, W.H., MOIN, P. & LEE, S. 1991 Subgrid-scale backscatter in turbulent and transitional flows. *Phys. Fluids* **3**, 1766–1771.
PIOMELLI, U., YU, Y. & ADRIAN, R.J. 1996 Subgrid-scale energy transfer and near-wall turbulence structure. *Phys. Fluids* **8**, 215–224.
PIROZZOLI, S., MODESTI, D., ORLANDI, P. & GRASSO, F. 2018 Turbulence and secondary motions in square duct flow. *J. Fluid Mech.* **840**, 631–655.
PLUNIAN, F., TEIMURAZOV, A., STEPANOV, R. & VERMA, M.K. 2020 Inverse cascade of energy in helical turbulence. *J. Fluid Mech.* **895**, A13.
POPE, S.B. 2001 *Turbulent Flows*. IOP Publishing.
POUQUET, A. & MININNI, P.D. 2010 The interplay between helicity and rotation in turbulence: implications for scaling laws and small-scale dynamics. *Phil. Trans. R. Soc. Lond.* **368**, 1635–1662.
POVITSKY, A. 2017 Three-dimensional flow with elevated helicity in driven cavity by parallel walls moving in perpendicular directions. *Phys. Fluids* **29**, 083601.
RECKTENWALD, I., ALKISHRIWI, N. & SCHRÖDER, W. 2009 PIV–LES analysis of channel flow rotating about the streamwise axis. *Eur. J. Mech. (B/Fluids)* **28**, 677–688.
RECKTENWALD, I., WELLER, T., SCHRÖDER, W. & OBERLACK, M. 2007 Comparison of direct numerical simulations and particle-image velocimetry data of turbulent channel flow rotating about the streamwise axis. *Phys. Fluids* **19**, 085114.
ROGERS, M.M. & MOIN, P. 1987 Helicity fluctuations in incompressible turbulent flows. *Phys. Fluids* **30**, 2662–2671.
SCHEELER, M.W., VAN REES, W.M., KEDIA, H., KLECKNER, D. & IRVINE, W.T.M. 2017 Complete measurement of helicity and its dynamics in vortex tubes. *Science* **357**, 487–491.
VALLIS, G.K. 2017 *Atmospheric And Oceanic Fluid Dynamics*. Cambridge University Press.
WALL, D.P. & NAGATA, M. 2006 Nonlinear secondary flow through a rotating channel. *J. Fluid Mech.* **564**, 25–55.
WANG, J.C., SHI, Y.P., WANG, L.P., XIAO, Z.L., HE, X.T. & CHEN, S.Y. 2012 Effect of compressibility on the small-scale structures in isotropic turbulence. *J. Fluid Mech.* **713**, 588–631.
WELLER, T. & OBERLACK, M. 2006 DNS of a turbulent channel flow with streamwise rotation – investigation on the cross flow phenomena. In *Direct and Large-Eddy Simulation VI* (ed. E. Lamballais, R. Friedrich, B.J. Geurts & O. Métais), ERCOFTAC, vol. 10, pp. 241–248. Springer.
WU, H. & KASAGI, N. 2004 Effects of arbitrary directional system rotation on turbulent channel flow. *Phys. Fluids* **16**, 979–990.
XIA, Z.H., SHI, Y.P. & CHEN, S.Y. 2016 Direct numerical simulation of turbulent channel flow with spanwise rotation. *J. Fluid Mech.* **788**, 42–56.
YAN, Z., LI, X.L., WANG, J.C. & YU, C.P. 2019 Effect of pressure on joint cascade of kinetic energy and helicity in compressible helical turbulence. *Phys. Rev.* E **99**, 033114.
YAN, Z., LI, X.L., YU, C.P., WANG, J.C. & CHEN, S.Y. 2020 Dual channels of helicity cascade in turbulent flows. *J. Fluid Mech.* **894**, R2.

YANG, Z.X., DENG, B.Q., WANG, B.C. & SHEN, L. 2018 The effects of streamwise system rotation on pressure fluctuations in a turbulent channel flow. *Phys. Fluids* **30**, 091701.

YANG, Z.X., DENG, B.Q., WANG, B.C. & SHEN, L. 2020*a* On the self-constraint mechanism of the cross-stream secondary flow in a streamwise-rotating channel. *Phys. Fluids* **32**, 105115.

YANG, Z.X., DENG, B.Q., WANG, B.C. & SHEN, L. 2020*b* Sustaining mechanism of Taylor–Görtler-like vortices in a streamwise-rotating channel flow. *Phys. Rev. Fluids* **5**, 044601.

YANG, Y.T., SU, W.D. & WU, J.Z. 2010 Helical-wave decomposition and applications to channel turbulence with streamwise rotation. *J. Fluid Mech.* **662**, 91–122.

YANG, Z.X. & WANG, B.C. 2018 Capturing Taylor–Görtler vortices in a streamwise-rotating channel at very high rotation numbers. *J. Fluid Mech.* **838**, 658–689.

YANG, Y.T. & WU, J.Z. 2012 Channel turbulence with spanwise rotation studied using helical wave decomposition. *J. Fluid Mech.* **692**, 137–152.

YOKOI, N. & YOSHIZAWA, A. 1993 Statistical analysis of the effects of helicity in inhomogeneous turbulence. *Phys. Fluids* **5**, 464–477.